# Heterojunction Modification for Highly Efficient Organic−Inorganic Perovskite Solar Cells

Konrad Wojciechowski,[†] Samuel D. Stranks,[†] Antonio Abate,[†] Golnaz Sadoughi,[†] Aditya Sadhanala,[‡] Nikos Kopidakis,[§] Garry Rumbles,[§] Chang-Zhi Li,[||] Richard H. Friend,[‡] Alex K.-Y. Jen,[||] and Henry J. Snaith*[,†]

[†]Clarendon Laboratory, University of Oxford, Parks Road, Oxford OX1 3PU, United Kingdom, [‡]Cavendish Laboratory, University of Cambridge, J. J. Thomson Avenue, Cambridge CB3 0HE, United Kingdom, [§]National Renewable Energy Laboratory, Denver West Parkway, Golden, Colorado 80401, United States, and [||]Department of Materials Science & Engineering, University of Washington, Seattle, Washington 98195, United States

ABSTRACT Organic−inorganic perovskites, such as $CH_3NH_3PbX_3$ (X = I, Br, Cl), have emerged as attractive absorber materials for the fabrication of low cost high efficiency solar cells. Over the last 3 years, there has been an exceptional rise in power conversion efficiencies (PCEs), demonstrating the outstanding potential of these perovskite materials. However, in most device architectures, including the simplest thin-film planar structure, a current−voltage response displays an "anomalous hysteresis", whereby the power output of the cell varies with measurement time, direction and light exposure or bias history. Here we provide insight into the physical processes occurring at the interface between the n-type charge collection layer and the perovskite absorber. Through spectroscopic measurements, we find that electron transfer from the perovskite to the TiO_2 in the standard planar junction cells is very slow. By modifying the n-type contact with a self-assembled fullerene monolayer, electron transfer is "switched on", and both the n-type and p-type heterojunctions with the perovskite are active in driving the photovoltaic operation. The fullerene-modified devices achieve up to 17.3% power conversion efficiency with significantly reduced hysteresis, and stabilized power output reaching 15.7% in the planar p−i−n heterojunction solar cells measured under simulated AM 1.5 sunlight.
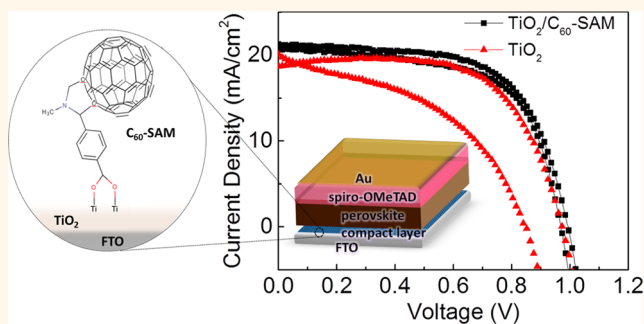
Organic−inorganic metal halide perovskite solar cells were reported for the first time between 2006 and 2009 by the work of Miyasaka and co-workers,[1,2] when they employed small $CH_3NH_3PbX_3$ (where X is I or Br) nanocrystals in replacement of ruthenium complex dyes in dye-sensitized solar cell architectures employing either a liquid electrolyte redox couple or polypyrrole carbon black composite solid-state hole conductor. Significant research into these materials did not occur until breakthroughs 3 years later when use of the molecular solid state hole transporting material, spiro-OMeTAD (2,2′,7,7′-tetrakis(N,N-di-4-methoxyphenylamino)-9,9′-spirobifluorene), produced much more efficient and more stable devices,[3,4] and even enabled completely new device architectures to be realized with the absence of mesoporous TiO_2.[4] Since then, metal−halide perovskite materials have garnered an explosion of interest due to their remarkable photovoltaic performance, low temperature and facile processing,[4−11] and even exhibiting efficient light emission and lasing properties.[12−14] Verified solar cell PCEs over 20% have been achieved,[15,16] with highest lab determined efficiencies of over 19%,[17] which places perovskite PV as one of the most promising and fastest growing of all photovoltaic technologies.
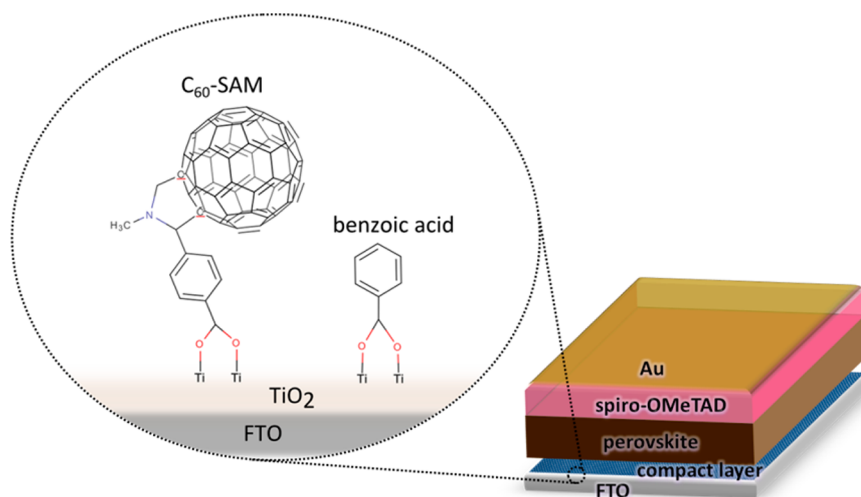
The devices are mostly based on hybrid organic−inorganic solution-processed polycrystalline $CH_3NH_3PbX_3$ films, where X is I, Br or Cl or a combination of halides.[4,5,18−21] The high performance is attributed to the favorable optoelectronic properties of these perovskites, such as appropriate bandgap, long electron and hole diffusion lengths,

Figure 1. Schematic of device structure and in the inset binding of SAMs to TiO_2 surface.

high crystallinity,[22−25] and low nonradiative decay rates.[13] These all stem from the remarkable ease with which the materials crystallize and the favorable defect chemistry, which is only just starting to be understood.[26−28] They can act as an n-type, p-type or even intrinsic (i-type) semiconductor material and, therefore, assume the roles of both light absorber and long-range charge transporter in a simple thin-film configuration.

Solar to electrical power conversion efficiencies are typically determined from current density−voltage (JV) curves measured under simulated sun light. The JV curves are obtained during light exposure by sweeping an applied bias across the terminals of the cell while measuring the current flowing in the external circuit. This is intended to closely represent the steady state power output of a solar cell at any given bias, and should not be dependent upon bias sweep rate or sweep direction. Perovskite devices often exhibit anomalous hysteresis in their current−voltage curves, with differences in the current measured in the forward and reverse scanning directions.[29,30] Hysteresis in most solar cells is due to the capacitance of the solar cell and should not be significant if the scan rate is slowed to a suitable level. For perovskite solar cells the hysteresis effect is particularly pronounced in planar heterojunction architectures, and unlike what would be expected from typical capacitive charging/discharging effects, the hysteresis can persist even at very slow scan rates.[16,29,31] To reach stabilized current output, the voltage step in some instances has to be held constant for hundreds of seconds, resulting in impractically slow scan rates required to determine a true "steady state" current voltage curve. This effect is problematic for universal and unambiguous characterization of photovoltaic performance of those devices and comparing efficiencies between changes in materials and device fabrication processes.

The hysteresis arises due to a change in the effective operation of the solar cell when held under forward bias or short-circuit conditions. The parameters internal to the cell which are different under these two conditions are electric field and charge density. Since the current generated and/or collected after holding the cells under forward bias is larger than under short-circuit, either the efficacy for charge collection at the electrodes is reduced at short-circuit, or the electron lifetime is reduced, or a combination of the two.[29] State-of-the-art perovskite devices typically utilize a thin and uniform compact TiO_2 layer as an electron-selective contact, and a p-type organic hole-conductor as the hole-selective contact.[17] Any bias induced changes to charge collection could either be due to a change to the bulk property of the perovskite, or due to a change to the nature of the contact (either at the surface of the perovskite, nature of interface states or the contact materials themselves).

Here, we investigate the contact between the perovskite and the planar n-type TiO_2 charge collection layer and find that electron transfer is not very effective. By modifying this contact with an organic electron accepting fullerene self-assembled monolayer (C_{60}-SAM) we significantly enhance electron transfer. We show that planar heterojunction perovskite solar cells incorporating the C_{60}-SAM-modified TiO_2, as illustrated schematically in Figure 1, result in a largely improved photovoltaic performance, a decrease in hysteretic behavior and a significant increase in the stabilized power output.

RESULTS AND DISCUSSION

The role of the n-type compact TiO_2 layer is to collect electrons and reflect holes. To investigate the ability of electrons in the perovskite to transfer across to the compact TiO_2, we measured time-resolved photoluminescence decays (Figure 2a) and the photoluminescence quantum efficiencies (PLQE; Table 1) of the perovskite films deposited upon TiO_2 compact layers and glass slides. The lifetime of the emission from the perovskite is only slightly reduced when coated on the

a)

b)
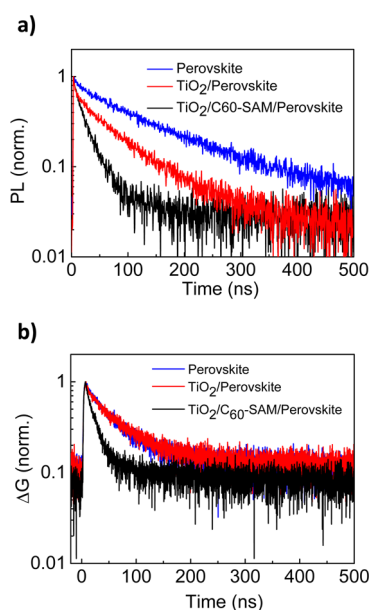
Figure 2. (a) Normalized photoluminescence decays following pulsed excitation (507 nm, 1 MHz, 0.03 μJ/cm^2/pulse) and (b) normalized time-resolved microwave conductivity (TRMC) decays following pulsed excitation (500 nm, 10 Hz, 0.1 μJ/cm^2/pulse) of perovskite both with and without electron quenching layers.

TABLE 1. PLQE Values of Perovskite Films with and without C$_{60}$-SAM Functionalization of the TiO$_2$

sample	PLQE (%)
No quencher	7.6
TiO$_2$	3.8
TiO$_2$/C$_{60}$-SAM	0.5

TiO$_2$ compact layer with the PLQE remaining half that of the perovskite film on glass. This suggests extremely poor or slow electron transfer to the TiO$_2$. This should be compared to the extremely fast quenching when the perovskite is coated with a fullerene derivative, as we have previously shown,[22,24] where the PL is almost entirely quenched. To corroborate the photoluminescence measurements, we have performed time-resolved microwave conductivity (TRMC) on similar samples. The figure of merit typically extracted from TRMC measurements under optical excitation is the product of the yield of free charge generation per absorbed photon, φ, with the sum of the mobilities of free charges, $\Sigma\mu$.[32] We find that the peak $\varphi\Sigma\mu$ product (at early time) as a function of absorbed flux does not depend (within experimental error) on the sample architecture (Supporting Information Figure S2a). This implies that the generation of mobile conductive charge occurs irrespective of interface, consistent with free carrier generation occurring spontaneously (on shorter than the nanosecond timescale) following light absorption within the bulk of the perovskite film. In particular, samples with spiro-OMeTAD on top of the perovskite film show very similar initial $\varphi\Sigma\mu_{t=0}$ to the neat perovskite film. Hole injection

to spiro-OMeTAD following photoexcitation of the perovskite is expected to be efficient[4,22] and microwave mobility of holes in the spiro-OMeTAD is expected to be much lower than that in the perovskite.[33] However, our data show no decrease of $\varphi\Sigma\mu_{t=0}$ with the addition of the spiro-OMeTAD, which suggests that the microwave conductivity signal is dominated by electrons in the perovskite. Since $\varphi\Sigma\mu_{t=0}$ is also the same for a perovskite film on glass and on TiO$_2$, we conclude that electron injection into the TiO$_2$ is quite inefficient, at least within the 5 ns excitation pulse used in the TRMC experiment. Efficient ultrafast electron injection to TiO$_2$ would result in decreased $\varphi\Sigma\mu$ values due to the low, microwave electron mobility in TiO$_2$.[34] Furthermore, we compare photoconductance transients measured by TRMC in Figure 2b, for perovskite films on glass and on compact TiO$_2$, which are essentially indistinguishable. If substantial electron transfer occurred from the perovskite to the TiO$_2$ we would expect a significant difference in the photoconductance decay profiles for these two samples, indicative of the removal of electrons from the perovskite films.[35] Since this is not observed, it again suggests that after photoexcitation in the perovskite, electron transfer to the compact TiO$_2$ is poor. Unexpectedly, the perovskite sample with a hole-quenching spiro-OMeTAD layer on top shows an even slower decay of the TRMC transient (Supporting Information Figure S2b). As mentioned earlier, we expect to observe efficient hole transfer to spiro-OMeTAD, and would hence expect to observe a faster TRMC transient decay if both electrons and holes were detected. However, the results are explicable if the hole mobility is significantly lower than the electron mobility within the perovskite film at the 10 GHz range. Then, following hole extraction[22] the lifetime of the electron conductivity signal would be extended since recombination is inhibited by the fact that the holes have been extracted from the perovskite film.

These results suggest that for the current planar heterojunction perovskite solar cells which employ compact TiO$_2$ as the electron collection layer, the major heterojunction generating the voltage and photocurrent is the perovskite:hole-transporter junction. Under illumination, the perovskite will transfer holes to the hole-conductor then accumulate electrons until the quasi-Fermi level for electrons within the perovskite is suitably low (close to vacuum) to allow a flow of electrons across the TiO$_2$ interface and enable a steady state current to flow.

Since we already know that fullerene molecules can act as a good acceptor of electrons on perovskites,[36−38] here we investigate the impact of modifying the compact TiO$_2$ with a fullerene self-assembled monolayer. The C$_{60}$-SAM we employ binds to the TiO$_2$ surface hydroxyl groups through the carboxylic acid anchoring group,[39−41] as we show in the schematic in Figure 1. In Supporting Information

Figures S1a–c, we present SEM images of modified and unmodified TiO$_2$ surfaces. We show the PL and TRMC data for perovskite films coated on C$_{60}$-SAM-modified TiO$_2$ in Figure 2. The PL quenching is dramatically enhanced, which is consistent with the C$_{60}$-SAM mono-layer enabling better extraction of photoinduced electrons from the perovskite. The TRMC traces also show a significant reduction in decay time upon modification, again consistent with effective electron transfer to the fullerene-modified TiO$_2$. Notably, we expect that the C$_{60}$-SAM-modified TiO$_2$ should only extract electrons, yet the rate of decay of the TRMC transient increases by an order of magnitude following photoexcitation. Again, if the 10 GHz hole-mobility was similar to the electron mobility, we would expect this transient to lengthen as the recombination processes was diminished. These results are once again consistent with the hole-mobility being lower than the electron mobility. In previous investigations,[22,24,35,43] the data have suggested that the long-range electron and hole mobilities are balanced, hence this discrepancy with the values predicted at 10 GHz warrants further investigation to determine if it is a property of the material or measurement. In particular, charge confinement effects and scattering associated with grain size. Recently it has been shown by DFT calculations that effective mass of electrons is lower than holes, which is in agreement with our findings of higher electron mobility.[42]

The above data are consistent with the fullerene-modified TiO$_2$ significantly enhancing the efficacy with which photoinduced electrons can flow out of the perovskite. The modification itself may also have an impact upon the TiO$_2$. It has been previously shown that crystalline TiO$_2$ contains inherent localized trap states due to under-coordinated surface Ti(IV) ions. Those states give an exponentially decreasing tail in the density of states below the conduction band.[44] Adsorption of electron-donating ligands at the surface, such as H$_2$O molecules, decreases the work function (shifts closer to vacuum) and reduces the number of available states in the sub-bandgap region. However, hydration does not saturate those sites entirely, since water adsorption is not stable and is difficult to control. To investigate the influence of C$_{60}$-SAM treatment on trap states in TiO$_2$ we performed photothermal deflection spectroscopy (PDS) measurements.[26,45,46] PDS is a technique which allows us to probe with high sensitivity the sub-bandgap optical absorption, and thus the trap states due to under-coordinated surface Ti(IV) ions. The slope of the absorption at the band edge defines the Urbach energy, and provides a measure for the degree of disorder of a material. During the first measurements we found that the spectrum of TiO$_2$ films modified with C$_{60}$-SAM showed a strong contribution from the fullerene (see Supporting Information Figure S3), which overlaps with the TiO$_2$ sub-bandgap absorption, and makes it difficult to probe any change
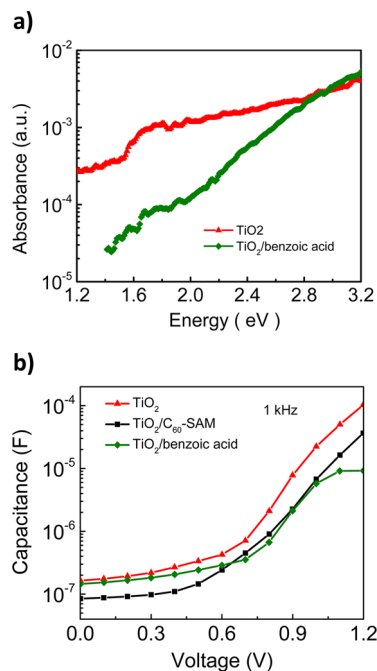

Figure 3. (a) PDS spectra of TiO$_2$ films, unmodified (red curve with triangles) and modified with a monolayer of benzoic acid (green curve with diamonds); (b) capacitance–voltage char-acteristics of TiO$_2$ films, unmodified (red curve with triangles), modified with a monolayer of C$_{60}$-SAM (black curve with squares), benzoic acid (green curve with diamonds).

in the TiO$_2$ density of states (DOS). However, the C$_{60}$-SAM is anchored to the TiO$_2$ surface *via* a benzoic acid group (see Figure 1), which is linked to the fullerene *via* a pyrrolidine derivative group (no π conjugation with the C$_{60}$), therefore we used benzoic acid to mimic the effect of the C$_{60}$-SAM anchoring group on the sub-bandgap absorption of TiO$_2$. In Figure 3a we compare PDS spectra of TiO$_2$ and TiO$_2$ modified with benzoic acid on quartz substrates. We observe a significant reduction in the sub-bandgap absorption in TiO$_2$ upon benzoic acid functionalization.

To show that the effect of the benzoic acid on the TiO$_2$ trap states is comparable to the C$_{60}$-SAM, we performed impedance measurements on simple diodes made by a stack of FTO/TiO$_2$/spiro-OMeTAD/Au layers, where the TiO$_2$ was modified with benzoic acid and C$_{60}$-SAM. We extracted capacitance–voltage char-acteristics at 1 kHz (Figure 3b). At this frequency a high variation of capacitance occurs with increasing bias voltage, which is indicative of charge accumulation at the compact layer and can represent its capacitance, which we show further evidence for in Supporting Information.[47,48] Upon assembling benzoic acid or C$_{60}$-SAM, which can be seen in the absorption in the sub-bandgap region, the capacitance of TiO$_2$ is clearly reduced. This confirms that the sub-bandgap DOS in the TiO$_2$ is reduced after modification with C$_{60}$-SAM. We note that benzoic acid reduces the capacitance even more effectively than the C$_{60}$-SAM. This effect could be explained by the contribution of fullerene in

the charge accumulation and observed capacitance, but it may also be due to the fact that small molecules like benzoic acid bind with a higher density as
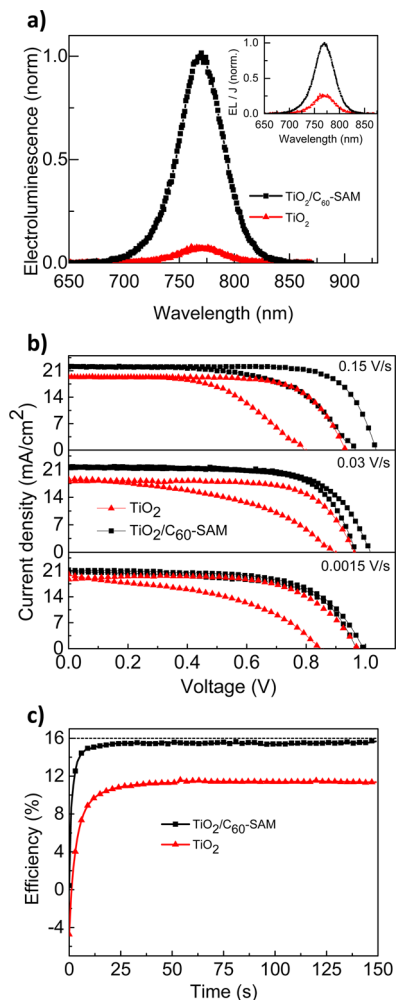
Figure 4. (a) Electroluminescence spectra from photovoltaic devices held at forward bias (1.1 V) containing C_{60}-SAM-modified (black curve with squares) and unmodified TiO_2 compact layer (red curve with triangles). The spectra presented are the peak EL emission following a slow rise (see Supporting Information Figure S5). Inset: EL spectra after accounting for differences in injected current density (EL/J). (b) JV curves of perovskite solar cells with C_{60}-SAM-modified (black curve with squares) and unmodified TiO_2 (red curve with triangles) compact layer obtained at the scanning rate of 0.15 V/s (top panel), 0.03 V/s (middle panel), and 0.0015 V/s (bottom panel). (c) Stabilized power output measured close to the maximum power point.

compared to the bulkier C_{60}-SAM. We have previously demonstrated a similar decrease in the overall capacitance of a solar cell upon C_{60}-SAM functionalization of mesoporous TiO_2.[39−41] However, in the previous instance we found that subsequent electron transfer to the mesoporous TiO_2 did not occur readily, and the reduced capacitance was interpreted as being due to blocking of the electron transfer to the TiO_2, and little change was observed with the benzoic acid. This is distinct from the effect which we are observing here with the compact TiO_2 layers in the planar junction. Presumably the electron density in the C_{60}-SAM is considerably enhanced in this instance enabling forward electron transfer.

We constructed complete planar heterojunction perovskite solar cells, both with and without the fullerene modification to the compact TiO_2. Before we present the solar cell results, we also measured the electroluminescence EL of the photovoltaic devices with and without C_{60}-SAM modification (Figure 4a). Nonradiative recombination is indicative of inefficient PV operation.[49] EL is a simple measurement to perform that can quickly give information about any changes to the radiative *versus* the nonradiative recombination. Here, we observe a 5- to 10-fold increase of the electroluminescence signal for a fullerene-modified sample compared to standard cell. We also find that the dark current density is higher for any given applied bias, but by a smaller factor of 2−3 with the C_{60}-SAM treatment (see Supporting Information Figure S5). This indicates that the EL efficiency has increased, and as such the nonradiative recombination at the heterojunction reduced with the C_{60}-SAM treatment. This observed increase of EL intensity also suggests that the functionalization has led to a reduction of interface defect sites, either on the TiO_2 or in the perovskite, which would otherwise cause nonradiative recombination of injected carriers. This is also consistent with recent results by Q. Wang et al., who suggested that fullerene can passivate trap states in the perovskite itself.[37]

Moving to the solar cell operation, in Figure 4b we present JV curves of the planar heterojunction perovskite solar cells with and without the C_{60}-SAM-modification. We show all the photovoltaic parameters extracted from the JV curves in Table 2.

TABLE 2. Photovoltaic Parameters Extracted from JV Curves presented in Figure 4a

|	scanning rate	0.15 V/s		0.03 V/s		0.0015 V/s	
	scanning direction	SC->FB	FB->SC	SC->FB	FB->SC	SC->FB	FB->SC
TiO_2/C_{60}-SAM	J_{sc} (mA/cm²)	22.0	22.1	21.7	21.6	21.3	20.7
	Eff (%)	12.5	17.3	15.0	14.7	13.4	12.8
	V_{oc} (V)	0.97	1.04	1.02	0.97	0.99	0.97
	FF	0.59	0.75	0.67	0.70	0.63	0.63
TiO_2	J_{sc} (mA/cm²)	19.3	19.3	18.6	18.0	20.1	18.7
	Eff (%)	8.5	12.7	7.6	12.1	7.5	12.2
	V_{oc} (V)	0.79	0.93	0.90	0.96	0.85	0.97
	FF	0.55	0.70	0.46	0.69	0.44	0.63

Upon modification there is a significant increase in all parameters. At the scanning rate of 0.15 V/s devices reach PCEs up to 17.3% on the forward bias to short-circuit scan (FB-SC). We show the results for a large batch of devices in Supporting Information Figure S6 and Table S1.

We present two scan directions, forward bias (FB) to short circuit (SC) and short circuit (SC) to forward bias (FB). For the C_{60}-SAM samples, when we decrease the scanning rate, the hysteresis for the cells with C_{60}-SAM-modified TiO_2 blocking layer becomes negligible, while it is still very pronounced for the standard unmodified planar heterojunction devices, even at scanning rates 100 times slower (0.0015 V/s, 934 s to scan the entire JV curve). We observe a small decline in fill factor in the fullerene-modified devices when the scanning rate is slower than 0.15 V/s. To corroborate the current voltage curves, we present stabilized power output close to the maximum power point, which reflects the true sustainable power conversion efficiency of the solar cell. Fullerene-modified devices exhibit a faster rise and significantly higher PCE, reaching 15.7% (Figure 4c).

To discriminate between the improved electron extraction and the reduced defect density as a result of incorporating the C_{60}-SAM, we fabricated cells with benzoic acid-modified TiO_2. We observed no improvement in device performance and persistent large hysteresis in JV curves, even at reduced scanning rates (Supporting Information Figure S7). This is consistent with the primary function of the C_{60}-SAM being to enhance electron extraction from the perovskite layer.

To summarize our observations, photoinduced electron transfer from the perovskite to the compact TiO_2 does not appear to occur efficiently. In the standard devices, good operation relies upon slow electron−hole recombination within the perovskite and at the perovskite-hole-transporter interface since a large electron density is likely to reside within the perovskite absorber. Upon modification with C_{60}-SAM, electron transfer is enhanced. At the same time, the C_{60}-SAM appears to reduce the sub band gap density of states in the TiO_2 and reduce the nonradiative recombination at the perovskite TiO_2 heterojunction. The solar cells are dramatically improved with this modification, and specifically the time to reach stabilized power output, and the magnitude of the stabilized power output, are improved.

We propose the following mechanism to explain these findings. Electron trap states at the interface (both in TiO_2 and perovskite) at the short-circuit condition are only partially filled and are likely to result in a depletion region on both sides of the interface, and pinning of the electron quasi-Fermi level (Figure 5) to the occupation level of the interface states. This would result in band bending within the perovskite layer and an electrostatic barrier for electron transfer across this interface. When the solar cells are under illumination
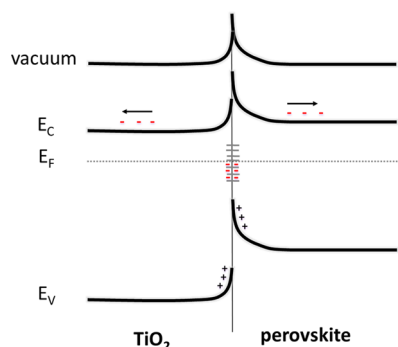
Figure 5. Schematic of the TiO_2/perovskite interface at the short-circuit condition in the dark, representing interface trap states causing the creation of a depletion region, Fermi level pinning and, in turn, band bending.

and forward bias, charge density can be built up, resulting in the filling of those states, a reduction in the degree of depletion and resulting in a flattening of the bands at this interface. When the scanning rate from forward bias to short-circuit is fast enough, deep trap states can remain filled since the lifetime of an electron in those states can be very long.[27] Passivation of the interface traps or permanent doping of the interfaces could overcome this problem and provide good selective charge collection. We note, however, that the time scale over which the photocurrent rises on the order of seconds. This is indicative of the sort of time required for long-range ion migration, rather than simply filling of defect sites.[50] We therefore postulate the phenomenon arises due to a combination of trapping and ion migration, but full understanding will require much more investigation.

CONCLUSION

In conclusion, we have demonstrated that the interface between the n-type collection layer and the $CH_3NH_3PbI_{3−x}Cl_x$ perovskite absorber has a strong influence on the operation of the solar cells. By modifying the surface of the TiO_2 compact layer with C_{60}-SAM molecules, we have observed a dramatic alteration to the operational mode of the solar cells. The standard devices are predominantly driven by the "i−p" perovskite hole−transporter heterojunction, whereas the fullerene-modified devices are driven by both the n−i and i−p heterojunctions in the p−i−n planar heterojunction solar cell. We find that the average PCEs increase from 11.5 to 14.8%, with a maximum stabilized power output of 15.7% for the C_{60}-SAM-modified devices. In addition to altering the operation of the solar cell, the C_{60}-SAM passivates or inhibits the formation of trap states at the interface, on the TiO_2 surface through the anchoring group, and on the perovskite side by the fullerene moiety, reducing the nonradiative recombination channels at this interface. This work significantly improves our understanding of the operation of perovskite solar cells, however it

indicates that many further improvements should be possible by focusing upon the nature of the interface between the n-type collection layer and the perovskite absorber.

METHODS

Materials and Device Fabrication. Unless otherwise stated, all materials were purchased from Sigma-Aldrich or Alfa Aesar and used as received. The C_{60}-substituted benzoic acid self-assembled monolayer (C_{60}-SAM) material was synthesized as described elsewhere.[40,41] Spiro-OMeTAD was purchased from Borun Chemicals and used as received. The synthesis of the perovskite, $CH_3NH_3PbI_{3-x}Cl_x$ has been reported elsewhere.[4]

Photovoltaic devices were fabricated on fluorine-doped tin oxide (FTO) coated glass (Pilkington, TEC7). Substrates were cleaned in hallmanex, then 10 min sonication in acetone, 10 min sonication in IPA, and 10 min of oxygen plasma etching. Compact layers were deposited by spin-coating a precursor solution (titanium isopropoxide, TTIP) in anhydrous ethanol (0.254 M) with the addition of a 0.02 M HCl, followed by sintering at 500 °C for 45 min. The functionalization of the compact layer was achieved by immersing hot TiO_2 substrates (when cooling down after sintering, temperature around 120 °C) in the C_{60}-SAM solution (0.1 mg/mL in chlorobenzene, filtered with 0.2 μm PTFE filter) for 24–36 h, followed by rinsing with chlorobenzene and drying for 10 min at 120 °C. After deposition of the compact layer, samples were transferred into a nitrogen-filled glovebox. Planar heterojunction perovskite films were prepared as reported elsewhere.[51] A precursor solution of the concentration of 400 mg/mL (CH_3NH_3I and $PbCl_2$, 3:1 molar ratio, in dimethyl-formamide (DMF)) was spin-coated at room temperature, followed by drying at room temperature for 30 min and annealing at 90 °C for 150 min, and 120 °C for 15 min. Surface passivation treatment was applied by spin-coating solution of iodopenta-fluorobenzene on top of formed perovskite, as reported by Abate et al.[52] The hole transporter was deposited by spin-coating an 8 wt % 2,2′,7,7′-tetrakis(N,N-di-4-methoxyphenylamine)-9,9-spirobifluorene (spiro-OMeTAD) in chlorobenzene with added tert-butylpyridine (tBP) and lithium bis(trifluoromethanesulfonyl)-imide (Li-TFSI) of 80 and 30 mol %, with respect to spiro-OMeTAD. Finally, 50 nm thick gold electrodes were deposited on top of devices by thermal evaporation at $\sim 10^{-6}$ bar, through a shadow mask.

For PDS measurements, all the films were deposited on IR-grade quartz substrates.

For PL measurements, all the films were deposited on microscope glass substrates. The perovskite layers were then sealed with a ~ 100 nm layer of the inert polymer poly(methyl methacrylate) (PMMA) (10 mg/mL, 1000 rpm) to reduce the impact of prolonged exposure to moisture.

Scanning Electron Microscopy. SEM images were obtained from a Hitachi S-4300 microscope.

Current Voltage Characteristics. JV characteristics of solar cells were measured under simulated AM1.5 100 mW.cm^{-2} sunlight (ABET Technologies Sun 2000) with a Keithley 2400 sourcemeter. The lamp was calibrated with an NREL-calibrated KG5 filtered silicon reference with a solar mismatch factor of 1.01. The active area of the device was defined by a metal mask with square aperture of the area of 0.0625 cm^2. The premasked active area of the solar cells was approximately 0.12 cm^2 nominally defined by the overlap area of the gold and FTO electrodes. Solar cells were masked for all the current voltage measurements.

Photoluminescence Measurements. Time-resolved PL measurements were acquired using a time-correlated single photon counting (TCSPC) setup (FluoTime 300, PicoQuant GmbH). Film samples were photoexcited using a 507 nm laser head (LDH-P-C-510, PicoQuant GmbH) pulsed at 1 MHz, with a pulse duration of 117 ps and fluence of 30 nJ/cm^2/pulse. The samples were exposed to the pulsed light source for ~ 10 min prior to measurement to ensure stable sample emission. The PL was collected using a high resolution monochromator and hybrid photomultiplier detector assembly (PMA Hybrid 40, PicoQuant GmbH).

Time-Resolved Microwave Conductivity. All samples were excited at 500 nm through the quartz substrate with 5 ns laser pulses from an optical parametric oscillator (Continuum Panther) pumped by the 355 nm harmonic of a Q-switched Nd:YAG laser (Continuum Powerlite) at a frequency of 10 Hz.

The sample is placed inside a resonance cavity at the end of an X-band (ca. 9 GHz) microwave waveguide and the transient change in photoconductance, $\Delta G(t)$, was measured via changes in the microwave power in the cavity, $\Delta P(t)$, due to absorption of microwaves by the photogenerated holes and electrons, and is given by

$$\Delta G(t) = -1/K(\Delta P(t)/P)$$

where K is a calibration factor determined experimentally from the resonance characteristics of the microwave cavity and the dielectric properties of the sample.[32] The peak photo-conductance, ΔG_{peak}, can be related to the product of the yield of free-carrier generation, φ, and the sum of the 9 GHz-frequency electron and hole mobilities, μ_e and μ_h, respectively (called $\Sigma \mu$), by

$$\Delta G_{peak} = \beta q_e I_0 F_A \varphi(\mu_e + \mu_h) = \beta q_e I_0 F_A \varphi \Sigma \mu$$

where $\beta = 2.2$ and is the ratio of the interior dimensions of the waveguide, q_e is the electronic charge, I_0 is the incident photon flux of the excitation laser pulse, and F_A is the fraction of absorbed laser pump photons by the sample.

Photoluminescence Quantum Efficiency Measurements. Photoluminescence quantum efficiency (PLQE) values were determined using a 532 nm CW laser excitation source (Suwtech LDC-800) to illuminate a sample in an integrating sphere (Oriel Instruments 70682NS), and the laser scatter and PL collected using a fiber-coupled detector (Ocean Optics Maya Pro). The spectral response of the fiber-coupled detector setup was calibrated using a spectral irradiance standard (Oriel Instruments 63358). An excitation intensity of ~ 200 mW/cm^2 was used for the measurements. PLQE calculations were carried out using established techniques.[53]

Electroluminescence Measurements. Electroluminescence measurements were carried out directly on the solar cells. Current–voltage characteristics were measured using a Keithley 2600 Source Measure Unit. A constant forward bias of 1.1 V was applied to the solar cells and the current monitored simultaneously. The electroluminescence was detected using a photomultiplier tube (PMT) detector (Fluorolog spectrofluorometer, Horiba Jobin-Yvon). All spectra were corrected for instrumental response using a calibration lamp of known emissivity.

Photothermal Deflection Spectroscopy. PDS is a highly sensitive surface averaged absorption measurement technique. Full details about this experiment are described elsewhere.[46] For this measurement, compact TiO_2 with and without surface modification has been prepared in the same manner as for the devices.

Impedance Measurements. Impedance measurements were taken using FRA-equipped PGSTAT-302N from Autolab; 20 mV AC sinusoidal signal with the frequency ranging from 1 MHz to 0.1 Hz was applied for each voltage bias (forward bias ranging from 0 to 1.2 V).

Conflict of Interest: The authors declare no competing financial interest.

REFERENCES AND NOTES

1. Kojimaa, A.; Teshimac, K.; Miyasakab, T.; Shirai, Y. Novel Photoelectrochemical Cell with Mesoscopic Electrodes Sensitized by Lead-Halide Compounds; 210th ECS Meeting, Cancun, Mexico, Oct. 29−Nov. 3, **2006**; 2014.

2. Kojima, A.; Teshima, K.; Shirai, Y.; Miyasaka, T. Organometal Halide Perovskites as Visible-Light Sensitizers for Photovoltaic Cells. *J. Am. Chem. Soc.* **2009**, *131*, 6050−6051.

3. Kim, H.-S.; Lee, C.-R.; Im, J.-H.; Lee, K.-B.; Moehl, T.; Marchioro, A.; Moon, S.-J.; Humphry-Baker, R.; Yum, J.-H.; Moser, J. E.; *et al.* Lead Iodide Perovskite Sensitized All-Solid-State Submicron Thin Film Mesoscopic Solar Cell with Efficiency Exceeding 9%. *Sci. Rep.* **2012**, *2*, 591.

4. Lee, M. M.; Teuscher, J.; Miyasaka, T.; Murakami, T. N.; Henry, J. Efficient Hybrid Solar Cells Based on Meso-Superstructured Organometal Halide Perovskites. *Science* **2012**, *338*, 643−647.

5. Liu, M.; Johnston, M. B.; Snaith, H. J. Efficient Planar Heterojunction Perovskite Solar Cells by Vapour Deposition. *Nature* **2013**, *501*, 395−398.

6. Burschka, J.; Pellet, N.; Moon, S.-J.; Humphry-Baker, R.; Gao, P.; Nazeeruddin, M. K.; Grätzel, M. Sequential Deposition as a Route to High-Performance Perovskite-Sensitized Solar Cells. *Nature* **2013**, *499*, 316−319.

7. Jeon, N. J.; Lee, H. G.; Kim, Y. C.; Seo, J.; Noh, J. H.; Lee, J.; Seok, S. I. O-Methoxy Substituents in Spiro − OMeTAD for Efficient Inorganic − Organic Hybrid Perovskite Solar Cells O-Methoxy Substituents in Spiro-OMeTAD for Efficient Inor- Ganic − Organic Hybrid Perovskite Solar Cells. *J. Am. Chem. Soc.* **2014**, *136*, 7837−7840.

8. Snaith, H. J. Perovskites: The Emergence of a New Era for Low-Cost, High-Efficiency Solar Cells. *J. Phys. Chem. Lett.* **2013**, *4*, 3623−3630.

9. Park, N.-G. Organometal Perovskite Light Absorbers Toward a 20% Efficiency Low-Cost Solid-State Mesoscopic Solar Cell. *J. Phys. Chem. Lett.* **2013**, *4*, 2423−2429.

10. Kim, H. S.; Im, S. H.; Park, N.-G. Organolead Halide Perovskite: New Horizons in Solar Cell Research. *J. Phys. Chem. C* **2014**, *118*, 5615−5625.

11. Gao, P.; Grätzel, M.; Nazeeruddin, M. K. Organohalide Lead Perovskites for Photovoltaic Applications. *Energy Environ. Sci.* **2014**, *7*, 2448−2463.

12. Tan, Z.-K.; Moghaddam, R. S.; Lai, M. L.; Docampo, P.; Higler, R.; Deschler, F.; Price, M.; Sadhanala, A.; Pazos, L. M.; Credgington, D.; *et al.* Bright Light-Emitting Diodes Based on Organometal Halide Perovskite. *Nat. Nanotechnol.* **2014**, *9*, 687−692.

13. Deschler, F.; Price, M.; Pathak, S.; Klintberg, L. E.; Jarausch, D.; Higler, R.; Hu, S.; Leijtens, T.; Stranks, S. D.; Snaith, H. J.; *et al.* High Photoluminescence Efficiency and Optically Pumped Lasing in Solution-Processed Mixed Halide Perovskite Semiconductors. *J. Phys. Chem. Lett.* **2014**, *5*, 1421−1426.

14. Xing, G.; Mathews, N.; Lim, S. S.; Yantara, N.; Liu, X.; Sabba, D.; Grätzel, M.; Mhaisalkar, S.; Sum, T. C. Low-Temperature Solution-Processed Wavelength-Tunable Perovskites for Lasing. *Nat. Mater.* **2014**, *13*, 476−480.

15. NREL. http://www.nrel.gov/ncpv/images/efficiency_chart.jpg.

16. Jeon, N. J.; Noh, J. H.; Kim, Y. C.; Yang, W. S.; Ryu, S.; Seok, S. I. Solvent Engineering for High-Performance Inorganic−organic Hybrid Perovskite Solar Cells. *Nat. Mater.* **2014**, *13*, 897−903.

17. Zhou, H.; Chen, Q.; Li, G.; Luo, S.; Song, T. -b.; Duan, H.-S.; Hong, Z.; You, J.; Liu, Y.; Yang, Y. Interface Engineering of Highly Efficient Perovskite Solar Cells. *Science* **2014**, *345*, 542−546.

18. Noh, J. H.; Im, S. H.; Heo, J. H.; Mandal, T. N.; Seok, S. I. Chemical Management for Colorful, Efficient, and Stable Inorganic− Organic Hybrid Nanostructured Solar Cells. *Nano Lett.* **2013**, *13*, 1764−1769.

19. Ryu, S.; Noh, J. H.; Jeon, N. J.; Kim, Y. C.; Yang, W. S.; Seoa, J.; Seok, S. I. Voltage Output of Efficient Perovskite Solar Cells with High Open-Circuit Voltage and Fill Factor. *Energy Environ. Sci.* **2014**, *7*, 2614−2618.

20. Ball, J. M.; Lee, M. M.; Hey, A.; Snaith, H. J. Low-Temperature Processed Meso-Superstructured Tp Ton-Film Perovskite Solar Cells. *Energy Environ. Sci.* **2013**, *6*, 1739.

21. Eperon, G. E.; Stranks, S. D.; Menelaou, C.; Johnston, M. B.; Herz, L. M.; Snaith, H. J. Formamidinium Lead Trihalide: A Broadly Tunable Perovskite for Efficient Planar Heterojunction Solar Cells. *Energy Environ. Sci.* **2014**, *7*, 982.

22. Stranks, S. D.; Eperon, G. E.; Grancini, G.; Menelaou, C.; Alcocer, M. J. P.; Leijtens, T.; Herz, L. M.; Petrozza, A.; Snaith, H. J. Electron-Hole Diffusion Lengths Exceeding 1 Micrometer in an Organometal Trihalide Perovskite Absorber. *Science* **2013**, *342*, 341−344.

23. Zhao, Y.; Nardes, A. M.; Zhu, K. Solid-State Mesostructured Perovskite CH 3 NH 3 PbI 3 Solar Cells: Charge Transport, Recombination, and Diffusion Length. *J. Phys. Chem. Lett.* **2014**, *5*, 490−494.

24. Xing, G.; Mathews, N.; Sun, S.; Lim, S. S.; Lam, Y. M.; Grätzel, M.; Mhaisalkar, S.; Sum, T. C. Long-Range Balanced Electron- and Hole-Transport Lengths in Organic-Inorganic $CH_3NH_3PbI_3$. *Science* **2013**, *342*, 344−347.

25. Wehrenfennig, C.; Eperon, G. E.; Johnston, M. B.; Snaith, H. J.; Herz, L. M. High Charge Carrier Mobilities and Lifetimes in Organolead Trihalide Perovskites. *Adv. Mater.* **2013**, *26*, 1584.

26. De Wolf, S.; Holovsky, J.; Moon, S.-J.; Löper, P.; Niesen, B.; Ledinsky, M.; Haug, F.-J.; Yum, J.-H.; Ballif, C. Organometallic Halide Perovskites: Sharp Optical Absorption Edge and Its Relation to Photovoltaic Performance. *J. Phys. Chem. Lett.* **2014**, *5*, 1035−1039.

27. Stranks, S. D.; Burlakov, V. M.; Leijtens, T.; Ball, J. M.; Goriely, A.; Snaith, H. J. Recombination Kinetics in Organic-Inorganic Perovskites: Excitons, Free Charge, and Subgap States. *Phys. Rev. Appl.* **2014**, *2*, 034007.

28. Kim, J.; Lee, S.; Lee, J. H.; Hong, K. The Role of Intrinsic Defects in Methylammonium Lead Iodide. *J. Phys. Chem. Lett.* **2014**, *5*, 1312−1317.

29. Snaith, H. J.; Abate, A.; Ball, J. M.; Eperon, G. E.; Leijtens, T.; Noel, N. K.; Stranks, S. D.; Wang, J. T.; Wojciechowski, K.; Zhang, W. Anomalous Hysteresis in Perovskite Solar Cells. *J. Phys. Chem. Lett.* **2014**, *17*, 1511−1515.

30. Yella, A.; Heiniger, L.-P.; Gao, P.; Nazeeruddin, M. K. Nanocrystalline Rutile Electron Extraction Layer Enables Low-Temperature Solution Processed Perovskite Photovoltaics with 13.7% Efficiency. *Nano Lett.* **2014**, *14*, 2591−2596.

31. Dualeh, A.; Moehl, T.; Tetreault, N.; Teuscher, J.; Gao, P.; Nazeeruddin, M. K.; Grätzel, M. Impedance Spectroscopic Analysis of Lead Iodide Perovskite-Sensitized Solid-State Sola Cells. *ACS Nano* **2013**, *8*, 362−373.

32. Savenije, T. J.; Ferguson, A. J.; Kopidakis, N.; Rumbles, G. Revealing the Dynamics of Charge Carriers in Polymer: Fullerene Blends Using Photoinduced Time-Resolved Microwave Conductivity. *J. Phys. Chem. C* **2013**, *117*, 24085−24103.

33. Poplavskyy, D.; Nelson, J. Nondispersive Hole Transport in Amorphous Films of Methoxy-Spirofluorene-Arylamine Organic Compound. *J. Appl. Phys.* **2003**, *93*, 341.

34. Kroeze, J. E.; Savenije, T. J.; Warman, J. M. Electrodeless Determination of the Trap Density, Decay Kinetics, and Charge Separation Efficiency of Dye-Sensitized Nanocrystalline TiO(2). *J. Am. Chem. Soc.* **2004**, *126*, 7608−7618.

35. Ponseca, C. S.; Savenije, T. J.; Abdellah, M.; Zheng, K.; Yartsev, A.; Pascher, T.; Harlang, T.; Chabera, P.; Pullerits, T.; Stepanov, A.; *et al.* Organometal Halide Perovskite Solar Cell Materials Rationalized: Ultrafast Charge Generation, High and Microsecond-Long Balanced Mobilities, and Slow Recombination. *J. Am. Chem. Soc.* **2014**, *136*, 5189−5192.

36. Docampo, P.; Ball, J. M.; Darwich, M.; Eperon, G. E.; Snaith, H. J. Efficient Organometal Trihalide Perovskite

Planar-Heterojunction Solar Cells on Flexible Polymer Substrates. *Nat. Commun.* **2013**, *4*, 2761.

37. Wang, Q.; Dong, Q.; Xiao, Z.; Yuan, Y.; Huang, J. Large Fill-Factor Bilayer Iodine Perovskite Solar Cells Fabricated by Low-Temperature Solution-Process. *Energy Environ. Sci.* **2014**, *7*, 2359–2365.

38. Malinkiewicz, O.; Yella, A.; Lee, Y. H.; Espallargas, G. M.; Graetzel, M.; Nazeeruddin, M. K.; Bolink, H. J. Perovskite Solar Cells Employing Organic Charge-Transport Layers. *Nat. Photonics* **2013**, *8*, 128–132.

39. Abrusci, A.; Stranks, S. D.; Docampo, P.; Yip, H.-L.; Jen, A. K.-Y.; Snaith, H. J. High Performance Perovskite-Polymer Hybrid Solar Cells *via* Electronic Coupling with Fullerene Mono-layers. *Nano Lett.* **2013**, *13*, 3124–3128.

40. Hau, S. K.; Yip, H.-L.; Acton, O.; Baek, N. S.; Ma, H.; Jen, A. K.-Y. Interfacial Modification to Improve Inverted Polymer Solar Cells. *J. Mater. Chem.* **2008**, *18*, 5113.

41. Hau, S. K.; Cheng, Y.-J.; Yip, H.-L.; Zhang, Y.; Ma, H.; Jen, A. K.-Y. Effect of Chemical Modification of Fullerene-Based Self-Assembled Monolayers on the Performance of Inverted Polymer Solar Cells. *ACS Appl. Mater. Interfaces* **2010**, *2*, 1892–1902.

42. Umari, P.; Mosconi, E.; De Angelis, F. Relativistic GW Calculations on $CH_3NH_3PbI_3$ and $CH_3NH_3SnI_3$ Perovskites for Solar Cell Applications. *Sci. Rep.* **2014**, *4*, 4467.

43. Giorgi, G.; Fujisawa, J.-I.; Segawa, H.; Yamashita, K. Small Photocarrier Effective Masses Featuring Ambipolar Transport in Methylammonium Lead Iodide Perovskite: A Density Functional Analysis. *J. Phys. Chem. Lett.* **2013**, *4*, 4213–4216.

44. Nunzi, F.; Mosconi, E.; Storchi, L.; Ronca, E.; Selloni, A.; Grätzel, M.; De Angelis, F. Inherent Electronic Trap States in TiO2 Nanocrystals: Effect of Saturation and Sintering. *Energy Environ. Sci.* **2013**, *6*, 1221.

45. Jackson, W. B.; Amer, N. M.; Boccara, a C.; Fournier, D. Photothermal Deflection Spectroscopy and Detection. *Appl. Opt.* **1981**, *20*, 1333–1344.

46. Kronemeijer, A. J.; Pecunia, V.; Venkateshvaran, D.; Nikolka, M.; Sadhanala, A.; Moriarty, J.; Szumilo, M.; Sirringhaus, H. Two-Dimensional Carrier Distribution in Top-Gate Poly-mer Field-Effect Transistors: Correlation between Width of Density of Localized States and Urbach Energy. *Adv. Mater.* **2014**, *26*, 728–733.

47. Kim, H.-S.; Mora-Sero, I.; Gonzalez-Pedro, V.; Fabregat-Santiago, F.; Juarez-Perez, E. J.; Park, N.-G.; Bisquert, J. Mechanism of Carrier Accumulation in Perovskite Thin-Absorber Solar Cells. *Nat. Commun.* **2013**, *4*, 2242.

48. Bisquert, J.; Bertoluzzi, L.; Mora-Sero, I.; Garcia-Belmonte, G. Theory of Impedance and Capacitance Spectroscopy of Solar Cells with Dielectric Relaxation, Drift-Diffusion Transport and Recombination. *J. Phys. Chem. C* **2014**, *118*, 18983–18991.

49. Miller, O. D.; Yablonovitch, E.; Kurtz, S. R. Strong Internal and External Luminescence as Solar Cells Approach the Shockley–Queisser Limit. *IEEE J. Photovoltaics* **2012**, *2*, 303–311.

50. Unger, E. L.; Hoke, E. T.; Bailie, C. D.; Nguyen, W. H.; Bowring, A. R.; Heumuller, T.; Christoforo, M. G.; McGehee, M. D. Hysteresis and Transient Behavior in Current-Voltage Measurements of Hybrid-Perovskite Absorber Solar Cells. *Energy Environ. Sci.* **2014**, *7*, 3690–3698.

51. Eperon, G. E.; Burlakov, V. M.; Docampo, P.; Goriely, A.; Snaith, H. J. Morphological Control for High Performance, Solution-Processed Planar Heterojunction Perovskite Solar Cells. *Adv. Funct. Mater.* **2013**, *24*, 151.

52. Abate, A.; Saliba, M.; Hollman, D. J.; Stranks, S. D.; Wojciechowski, K.; Avolio, R.; Grancini, G.; Petrozza, A.; Snaith, H. J. Supramolecular Halogen Bond Passivation of Supramolecular Halogen Bond Passivation of Organic-Inorganic Halide Perovskite Solar Cells. *Nano Lett.* **2014**, *14*, 3247–3254.

53. Mello, J. C. de; Wittmann, H. F.; Friend, R. H. An Improved Experimental Determination of External Photolumines-cence Quantum Efficiency. *Adv. Mater.* **1997**, *9*, 230–232.